ORIGINAL PAPER: NANO-STRUCTURED MATERIALS (PARTICLES, FIBERS, COLLOIDS, COMPOSITES, ETC.)

V$_2$O$_3$/C composite fabricated by carboxylic acid-assisted sol–gel synthesis as anode material for lithium-ion batteries
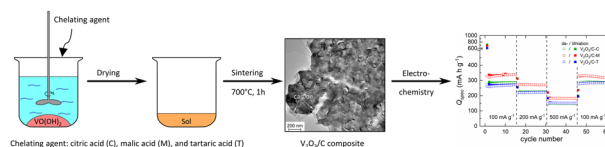
G. S. Zakharova[1] · E. Thauer [ID][2] · A. N. Enyashin[1] · L. F. Deeg[2] · Q. Zhu[3] · R. Klingeler[2,4]

Abstract

The potential battery electrode material V$_2$O$_3$/C has been prepared using a sol–gel thermolysis technique, employing vanadyl hydroxide as precursor and different organic acids as both chelating agents and carbon sources. Composition and morphology of resultant materials were characterized by X-ray diffraction, Raman spectroscopy, scanning and transmission electron microscopies, physical sorption, and elemental analysis. Stability and electronic properties of model composites with chemically and physically integrated carbon were studied by means of quantum-chemical calculations. All fabricated composites are hierarchically structured and consist of carbon-covered microparticles assembled of polyhedral V$_2$O$_3$ nanograins with intrusions of amorphous carbon at the grain boundaries. Such V$_2$O$_3$/C phase separation is thermodynamically favored while formation of vanadium (oxy)carbides or heavily doped V$_2$O$_3$ is highly unlikely. When used as anode for lithium-ion batteries, the nanocomposite V$_2$O$_3$/C fabricated with citric acid exhibits superior electrochemical performance with an excellent cycle stability and a specific charge capacity of 335 mAh g^{-1} in cycle 95 at 100 mA g^{-1}. We also find that the used carbon source has only minor effects on the materials' electrochemical performance.

Graphical Abstract

✉ E. Thauer
elisa.thauer@kip.uni-heidelberg.de

1   Institute of Solid State Chemistry, Ural Division, Russian Academy of Sciences, Yekaterinburg, Russia

2   Kirchhoff Institute of Physics, Heidelberg University, Heidelberg, Germany

3   School of Material Science and Engineering, Wuhan University of Technology, Wuhan, China

4   Centre for Advanced Materials, Heidelberg University, Heidelberg, Germany

Highlights

- V_2O_3/C composites were synthesized by a facile sol–gel thermolysis method.
- Citric acid, malic acid, and tartaric acid have been applied as both the chelating agents and as carbon source to produce V_2O_3/C composites for the first time.
- DFT calculations confirmed preference of phase separation in C-doped V_2O_3.
- V_2O_3/C composites as anode material exhibit an excellent cycle stability.

1 Introduction

Vanadium trioxide V_2O_3 has been widely studied in fundamental research since the first reports on its metal-to-insulator transition [1]. Regarding application, due to its high theoretical capacity (1070 mAh g^{-1}), low cost, and non-toxicity V_2O_3 is well recognized as a promising anode material for rechargeable lithium-ion batteries (LIBs) [2–4]. However, the practical use of the bulk V_2O_3 as anode materials in LIBs is greatly hindered due to huge volume changes appearing upon electrochemical cycling [5]. A variety of functionalization options has been explored to overcome this issues: incorporation of carbon containing compounds yielding composite materials including the preparation of nanosized materials with the different morphology [6, 7], doping with nitrogen and sulfur [8–10], as well as a design of three-dimensional nanostructures providing shorter lithium-ion/electron diffusion distances as well as more stable structures preventing deterioration of electrodes during the discharge/charge processes [11–16].

Both the preparation process and the post-treatment conditions have a significant influence on the electrochemical performances of V_2O_3/C hybrid materials as an anode material. For example, V_2O_3/C composites prepared by a NaCl template-assisted freeze-drying strategy deliver a capacity of 706 mAh g^{-1} at 5 A g^{-1}, after 2000 cycles [17], while electrospun materials show 100 mAh g^{-1} at 5000 A g^{-1} after 5000 cycles [18]. Among different kinds of carbon materials, there is a variety of reports using graphene oxide (rGO) as the carbon source [5, 19, 20], among them a polymer-pyrolysis made material with ~780 mAh g^{-1} over 100 cycles at 200 mA g^{-1} [21] and V_2O_3/rGO with 823 mAh g^{-1}, at 0.1 A g^{-1} [22]. Other V_2O_3/C composites have been fabricated by solvothermal synthesis using ethylene glycol as the carbon source (474 mAh g^{-1} at 0.5 A g^{-1} after 400 cycles) [23], a hydrothermal route and subsequent calcinations (283 mAh g^{-1} at 25 A g^{-1}) [24].

Here we report for the first time a sol–gel process with post-annealing treatment to synthesize a V_2O_3/C composite material using citric acid, tartaric acid, and malic acid as both the chelating agents and the carbon sources. In general, the sol–gel method has been extensively used to synthesize electrode materials due to their unique advantages such as low synthesis temperature, high purity and high homogeneous structure, and good electrochemical property of the synthesized product [25–28]. Our work shows that it can be exploited as facile method to synthesize hierarchically structured V_2O_3/C nanocomposite and we investigate in detail the influence of different carboxylic acids on the phase composition, morphology, and electrochemical properties of the products.

2 Experimental

2.1 Materials

Vanadyl sulfate hydrate $VOSO_4 \cdot nH_2O$ (97% $VOSO_4$), ammonium hydroxide solution (28% NH_3 in H_2O), tartaric acid ($C_4H_6O_6$), malic acid ($C_4H_6O_5$), and citric acid ($C_6H_8O_7$) with analytical grade were purchased from Sigma-Aldrich and used without any further purification.

2.2 Synthesis of V_2O_3/C composites

V_2O_3/C composites were prepared using the sol–gel thermolysis process. The typical synthesis process is briefly described as follows. First, vanadyl hydroxide $VO(OH)_2$ precursor was prepared. According to the synthetic procedure, 7.95 g $VOSO_4 \cdot nH_2O$ was dissolved in 400 mL of deionized H_2O using the magnetic stirring at room temperature, then ammonium hydroxide solution was added dropwise to adjust the pH value of the mixture so that it equals to 4. The brown precipitate was collected by centrifugation and washed several times with water, ethanol, and dried in air to obtain the $VO(OH)_2$ powder products. Second, $VO(OH)_2$ and carboxylic acid (citric acid, malic acid or tartaric acid) were weighed according to the molar ration of 1:1 and mixed well with each other in deionized 60 mL water under constantly stirring. The mixture then came to be a blue solution. The blue solution was evaporated at 80 °C for ~4 h, with a magnetic stirrer sequentially stirring to obtain a clear viscous sol and was subsequently dried to form a gel. The gel was further dried in a vacuum oven at 50 °C for 16 h, which led to a blue powder. Finally, the powder was sintered under a flow of N_2 gas at 400–700 °C for 1 h to obtain the V_2O_3/C composites. Depending on the type of the carboxylic acids, the resulting materials are denoted henceforth as V_2O_3/C-C, V_2O_3/C-M,

and V_2O_3/C-T, where carboxylic acid is citric acid, malic acid, and tartaric acid, respectively.

2.3 Characterization

X-ray diffraction (XRD) patterns were obtained using a Bruker AXS D8 Advance Eco diffractometer using CuKα radiation and applying the step size of $\Delta 2\theta = 0.02°$. The morphology of the powder was determined by a ZEISS Leo 1530 scanning electron microscope (SEM) as well as JEOL JEM 2100 and JEMe200 CX high-resolution transmission electron microscopes (HRTEM). The thermogravimetric analysis with the heating rate of 10 K min^{-1} under flowing air was carried out using a STA 449 F_3 Jupiter thermo-analyzer (Netzsch) coupled with a QMS 403 mass spectrometer (TG-DSC-MS). The specific surface area and pore volume of the samples were measured by a surface area and porosity analyzer (Gemine VII, Micromeritics). The content of carbon was examined by elemental chemical analysis (CA) using Vario MICRO Cubes (Elementar). Prior to N_2 physisorption data collection, the samples were degassed at 100 °C under vacuum for 1.5 h. The specific surface area, pore size distribution, and pore volumes were obtained by means of the Brunauer–Emmett–Teller (BET) method and the Barrett–Joyner–Halenda model from the adsorption branches of the isotherms. Raman spectra were measured with a Renishaw U1000 spectroscope at a laser wavelength of 532 nm.

2.4 Computational details

All quantum-chemical calculations of the V_2O_3/C composite systems were performed within the framework of the self-consistent-charge density-functional tight-binding method (SCC-DFTB) [29, 30]. Atomic positions in both the supercells of the bulk V_2O_3 doped by carbon and the supercells of a slab V_2O_3(0001) contacting with graphene were optimized using the conjugate gradient algorithm within periodic boundary conditions in Γ-point approximation. Self-consistent calculations were performed until the maximal residual components for the total energy of 10^{-3} eV atom^{-1} and for the interatomic force component of 10^{-2} eV Å^{-1}. The lattice parameters optimized within these conditions for the bulk V_2O_3 are in a fair agreement with the experimental values, being overestimated by 3% ($a = 5.07$ Å, $c = 14.25$ Å).

As the progenitor of all the model V_2O_3/C composites the pre-optimized supercell $2a \times 2a \times 1c$ of bulk V_2O_3 was selected. Several possible variants for distribution of carbon impurities within V_2O_3 lattice have been accounted: substitutional single C atoms within V or O sublattices; substitutional C_2 dimers at neighbor sites within V or/and O sublattices; interstitial single C atoms or C_2 dimers; graphene sheet on a V_2O_3 surface. The relative stability of these V_2O_3/C composites with relaxed internal geometry was analyzed using the energy of formation ΔE relative to corresponding mechanistic mixture of the bulk V_2O_3, graphite and molecular CO. Positive and negative ΔE values point to endo- and exothermic formation reaction, respectively.

2.5 Electrochemical measurements

The electrochemical measurements of the samples were performed with a VMP3 potentiostat (Bio-Logic SAS) at 25 °C using Swagelok-type half cells with lithium metal foil (Alfa Aesar) as counter electrode [31]. The electrodes were separated by two layers of glass fiber separator (Whatman GF/D) that was soaked with 200 μL of a 1 M LiPF$_6$ salt solution in 1:1 ethylene carbonate and dimethyl carbonate (Merck Electrolyte LP30). The working electrode consists of active material, carbon black (Super C65, Timcal) and polyvinylidene fluoride binder (Solvay Plastics) in a weight ratio of 75:15:10. The powders were mixed in N-methyl-2-pyrrolidone (NMP, Sigma-Aldrich) and stirred for at least 12 h. After evaporating most of the NMP under vacuum the spreadable slurry was deposited on circular Cu meshes (diameter 10 mm) with a mass loading of about 0.4–0.5 mg cm^{-2}. Afterward, the electrodes were dried under vacuum, pressed with a spindle press by hand and then dried again. The preparation of the electrodes and the cell assembly were done in a glovebox filled with argon (O_2/$H_2O < 5$ ppm). The calculation of the specific capacity is based on the total mass weight of the composites V_2O_3/C.

3 Results and discussion

XRD patterns of the V_2O_3/C composites prepared using different carboxylic acids at different temperatures are depicted in Fig. 1a. All samples obtained after annealing at temperatures below 700 °C are amorphous according to the XRD patterns as demonstrated by the example of the V_2O_3/C-C composite. Annealing at 700 °C leads to the appearance of distinguished XRD patterns, which can be undoubtedly attributed to V_2O_3 without any impurities. The lattice of V_2O_3 within the as-prepared V_2O_3/C composites has rhombohedral crystalline structure and belongs to the R-3c space group. For all crystalline V_2O_3/C materials reported here, the lattice parameters derived from the XRD data are listed in Table 1. The results are found close to the reported values for V_2O_3 [ICSD No. 94768]. The XRD patterns however display rather broad and low-intense diffraction peaks, which may be attributed to both a poor crystallinity or/and to a small crystal size of primary V_2O_3 particles present in the composites. Using Scherrer's equation enables estimating the average crystallite sizes of V_2O_3
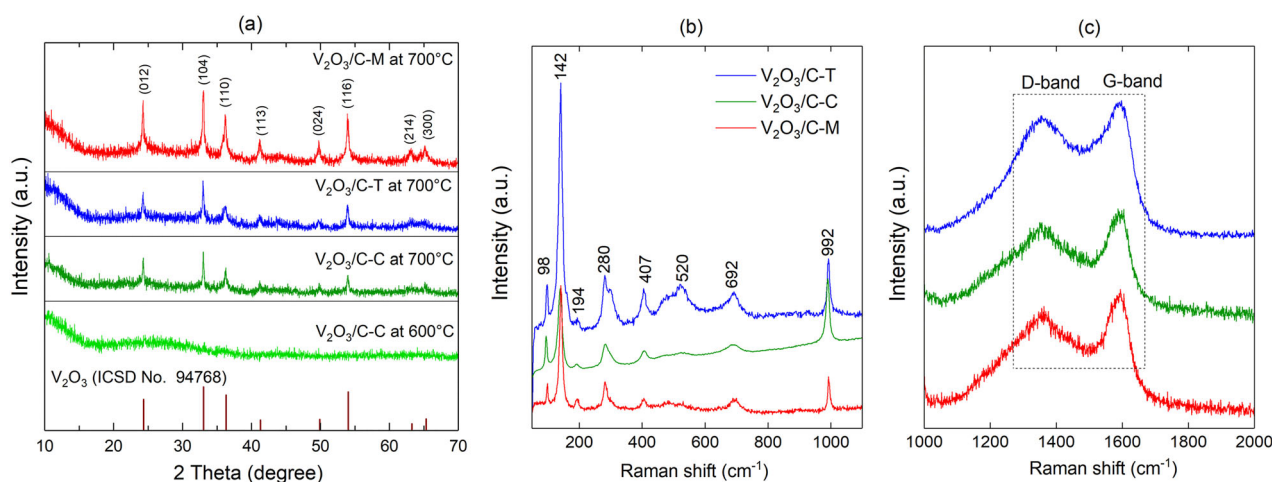
Fig. 1 a XRD patterns and Raman spectra in the range of **b** 50–1100 cm^{-1} and **c** 1000–2000 cm^{-1} of the V$_2$O$_3$/C composites fabricated using different carboxylic acids: citric acid (V$_2$O$_3$/C-C), tartaric acid (V$_2$O$_3$/C-T), and malic acid (V$_2$O$_3$/C-M)

Table 1 Lattice parameters, crystallite sizes from XRD, results of BET analysis, and carbon content of the V$_2$O$_3$/C composites synthesized at 700 °C. The last row shows lattice parameters from the literature

Samples	Lattice parameters		Crystallite size (nm)	S_{BET} (m^2 g^{-1})	Carbon content (wt%)	
	a (Å)	c (Å)			TG	CA
V$_2$O$_3$/C-C	4.9907	13.8858	34 (10)	1.8	27.0	26.3 (5)
V$_2$O$_3$/C-M	4.9659	13.9956	28 (5)	5.8	20.6	20.3 (5)
V$_2$O$_3$/C-T	4.9533	14.0280	31 (8)	6.7	16.8	19.6 (5)
V$_2$O$_3$ (ICSD No. 94768)	4.95254	14.0038	–	–	–	–

particles:

$$D_{hkl} = K\lambda/\Delta(2\theta_{hkl})\cos 2\theta_{hkl}, \tag{1}$$

where D_{hkl} is the extent of the crystal perpendicular to the reflecting hkl-crystal plane, K is a constant depending on the crystal shape which can be approximated to 0.9, λ is the wavelength of the applied CuKα radiation, $\Delta(2\theta_{hkl})$ is the full width at half-maximum of the diffraction peak, and θ_{hkl} is the Bragg angle. The average crystallite sizes of V$_2$O$_3$ particles obtained from the analysis of the (012), (104), (110), and (116) reflexes are presented in Table 1. All materials exhibit nanosized primary particles with similar size. Obviously, the crystallite size does not seem to be affected by the chelating agent, which was also observed for other oxide systems, for example, Y$_3$Fe$_5$O$_{12}$ and Y$_2$O$_3$ synthesized by sol–gel technique with citric, malic, or tartaric acid [32, 33]. This phenomenon is attributed to the space steric effect of the organic acids playing the role of the chelating agent [34]. The chelating ability of carboxylic acids depends on the presence of the carboxylic –COOH groups. Citric acid in comparison with both malic acid and tartaric acid has three –COOH

groups, which promote the formation of vanadium-ligand bonds, the formation of a chelate complex, and the growth of crystallites. However, the intermolecular steric hindrances are formed between the citric acid molecules and metal oxide due to the large molecular weight of the citric acid. A large space steric effect hinders close contact between the chelating agent and vanadium oxide that does not favor the growth of V$_2$O$_3$ particles. The main difference in the XRD patterns of the three composites is the relative intensity of the V$_2$O$_3$ reflexes. For the composite prepared using malic acid the ratio of the area of all crystalline peaks to the total area of the diffractogram is slightly higher than those for V$_2$O$_3$/C-C and V$_2$O$_3$/C-T indicating higher crystallinity of V$_2$O$_3$. This shows that malic acid is an eminent chelating agent to synthesize V$_2$O$_3$/C composite with higher crystallinity. Similar results were also observed in the synthesis of LiV$_3$O$_8$ prepared by sol–gel method and post-annealing treatment with citric, malic, and tartaric acid as chelating agents [35].

Raman spectroscopy provides further information about the structure of V$_2$O$_5$ and also on the carbon in the V$_2$O$_3$/C composites. All peaks shown in Fig. 1b located below 1000 cm^{-1} can be attributed to V–O vibrations of V$_2$O$_5$ in agreement with the literature values [36]. Evidently, V$_2$O$_3$ is partially oxidized to V$_2$O$_5$ under the laser irradiation during the Raman measurement in air [37] and therefore, the spectra also show characteristic Raman modes of the V$_2$O$_5$ phase. In addition, two broad peaks at ~1350 cm^{-1} and ~1600 cm^{-1} are clearly observed in the spectra of V$_2$O$_3$/C composites (Fig. 1c). The band at ~1600 cm^{-1} labeled as the G-band is related to the in-plane vibration of sp^2 hybridized carbon atoms [38–40], while the one at about 1350 cm^{-1} labeled as the D-band is associated to the breathing mode of sp^2 atoms in rings and only becomes active in the presence of defects [38–40]. The peaks of D- and G-bands are broad implying that carbon possesses high structural disorder [39, 41, 42]. The ratio of the
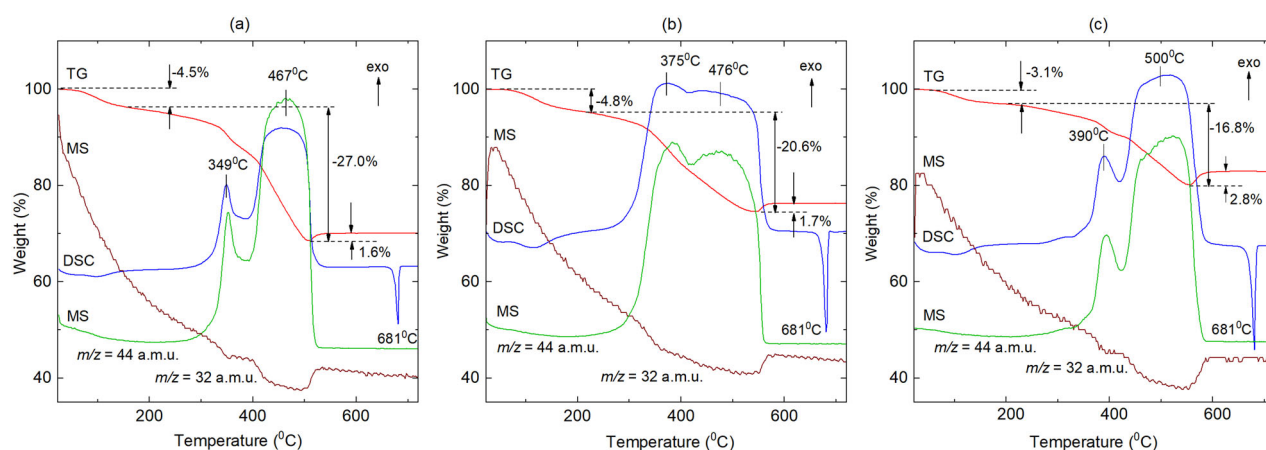
Fig. 2 Thermogravimetric (red), DSC (blue), and mass-spectroscopy (green, brown) curves of V_2O_3/C composites prepared using **a** citric acid, **b** malic acid, and **c** tartaric acid

maximum intensity of both peaks (I_D/I_G) of the V_2O_3/C composites, obtained by using citric acid, malic acid, and tartaric acid, are calculated to be 0.82, 0.83, and 0.87, respectively. In comparison with citric acid and malic acid as the chelating agent, this ratio is for V_2O_3/C-T composite slightly higher indicating less defects and disorder in the carbon component [38].

Thermogravimetric analyses coupled with mass-spectroscopy confirm the presence of carbon and allow to derive the carbon content in the V_2O_3/C composites under study (Fig. 2). The TG-DSC-MS curves of the composites prepared by citric acid (Fig. 2a), malic acid (Fig. 2b), and tartaric acid (Fig. 2c) are very similar. For all three composites, the weight loss proceeds stepwise. In the first step ranged from room temperature to about 180 °C, there is a weak endothermic peak signaling the vaporization of adsorption water. The corresponding weight loss is about 3.1−4.8 wt%. A second step ranging from 200 to 560 °C implies two strong exothermic peaks, which are associated with the vigorous combustion reactions of the carbon component in the composites and the completion of the crystallization reaction. The release of carbon dioxide CO_2 is confirmed by two intense peaks from molecular ion CO_2^+ with $m/z = 44$ a.m.u. in the mass spectra. Seemingly, the existence of this double exotherm with well-resolvable temperature maxima is due to the different states of carbon in the composites. A last feature is observed from ~500 to 730 °C. Here, there is a weight gain of 1.6, 1.7 and 2.8 wt% for V_2O_3/C-C, V_2O_3/C-M, V_2O_3/C-T samples, respectively, upon heating. This process is attributed to the oxidation of V^{3+} ions to V^{5+} and results in the formation of V_2O_5 as a final thermolysis product. The mass-spectroscopy curves reveal that the main gaseous product in this temperature regime is the molecular ion O_2^+ with $m/z = 32$ a.m.u. The endothermic peak at 681 °C is attributed to the melting of V_2O_5. According to the thermogravimetric analysis, the

content of carbon in the samples amounts to 27.0, 20.6, 16.8 wt% for V_2O_3/C-C, V_2O_3/C-M, V_2O_3/C-T, respectively. The results of the TG analyses fully agree with carbon content determined by CA (Table 1).

The morphologies of the V_2O_3/C powders synthesized from citric acid, malic acid, and tartaric acid as carbon source are similar. All of them show micrometer sized chunks (Fig. S1) that are decorated with flake-like particles with the average flake size of 100–300 nm and 30–40 nm in thickness (Fig. 3a–c). In addition, the detailed microstructure of the V_2O_3/C-C composite studied by TEM (Fig. 3d) displays a block-like architecture of particles on the nanometer scale. The TEM images also show an amorphous carbon layer of up to 100 nm in thickness. Nanoparticles with the shape of edge-shared polyhedra are uniformly and tightly anchored to an amorphous carbon matrix (Fig. 3e). The lattice fringes with spacing of 0.37 nm corresponds to the (012) plane of the rhombohedral V_2O_3 phase. The corresponding ring-like selected-area electron diffraction (SAED) pattern (Fig. 3f) indicates that the as-synthesized composite is a polycrystalline phase indexed to V_2O_3, which is consistent with the XRD results presented above. Textural properties of the differently prepared V_2O_3/C composites as obtained from nitrogen adsorption and desorption studies and their analysis are shown in Fig. S2 and in Table 1. According to the IUPAC classification, the nitrogen adsorption/desorption isotherms display a type IV behavior [43].

In summary, analysis of XRD, SEM, TEM, and BET data provides solid evidence that the materials exhibit tightly bound, yet, separated V_2O_3 and carbon phases. However, doping of carbon into the V_2O_3 lattice cannot be completely excluded, since it remains undetectable by these methods. Therefore, quantum-chemical DFTB calculations have been employed to estimate tendency of the V_2O_3 lattice to host substitutional and/ or interstitial carbon impurities. Several model variants of single and paired carbon atoms hosted at O- or V sites or as
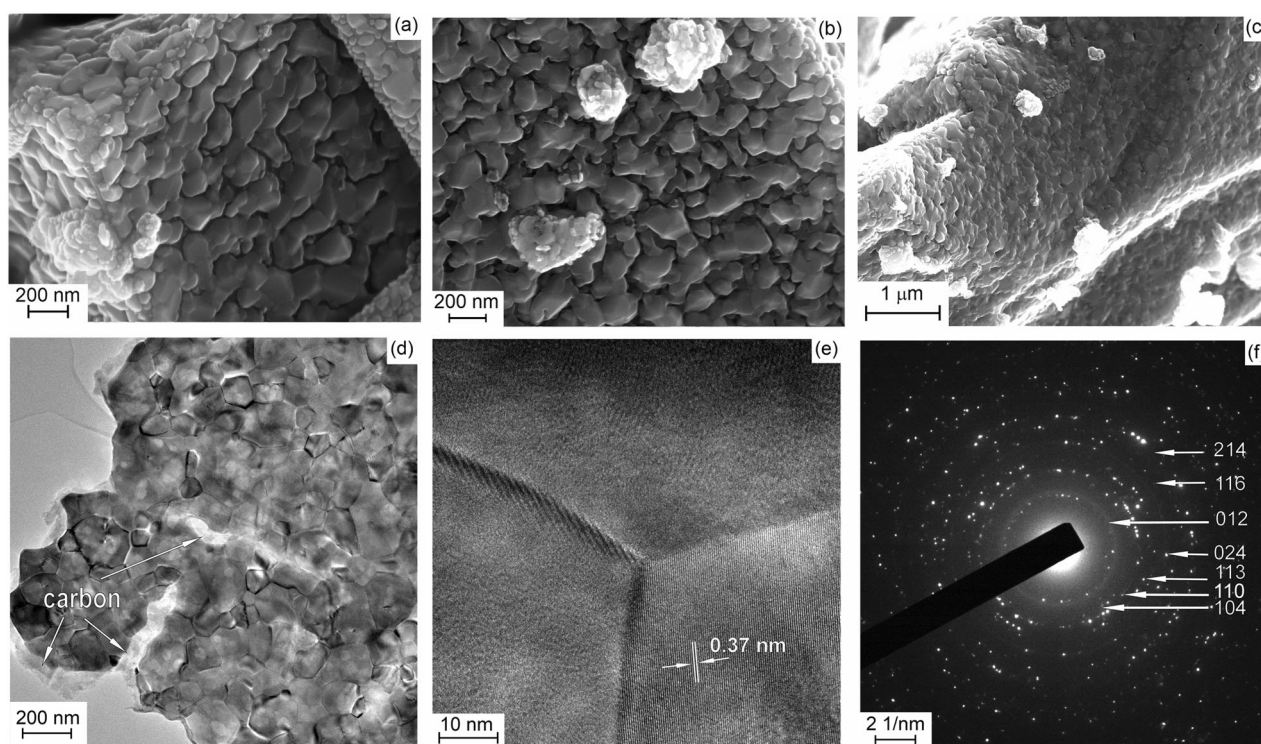
Fig. 3 SEM images of V_2O_3/C composites prepared with the different carboxylic acids: **a** citric acid, **b** malic acid, and **c** tartaric acid. **d** TEM, **e** HRTEM images, and **f** corresponding SAED pattern of V_2O_3/C-C composite

interstitials have been accounted (Table S1). An essential difference in their relative thermodynamic stabilities is established after comparison of their formation energies ΔE. There are a few important inferences. Namely, substitution of single O atoms by C atoms within V_2O_3, accompanied by emergence of carbide-like V–C bonding, is endothermic. Moreover, clusterization of such C atoms is even less favorite. Implantation of interstitial C atoms is also characterized by endothermic energies irrespective of the carbons' mutual distribution.

The energetically most beneficial and even exothermic carbon distribution has been found for the variants of cooperative substitution of either two neighboring V atoms or an VO unit (see Table S1). Optimized structures including these defects undergo a considerable evolution, compared to their initial geometries, which is accompanied by a contraction in the neighborhood of the defect, i.e., by the appearance of a nanoscopic cavity within the bulk of V_2O_3. Particularly, substitution of neighboring V and O atoms leads to the formation of acetylide-like dimers bound via an atom to two V atoms (Table S1, defect type 8). Though, the energetically most beneficial cooperative substitution is found to be on two neighboring V sites, which results in the formation of CO molecules within nanoscopic cavity. Depending on the initial positions of substituting C atoms, the final structure contains either two CO molecules (Table S1, defect type 10) or a single CO molecule and a carbonate-like group (Table S1, defect type 11, and Fig. S3).

Beside the formation of molecular-like carbon species or carbon oxides, the release of free carbon in bulk quantities like a graphene sheet on the V_2O_3(0001) surface should be also an exothermic reaction (Table S1, defect type 14, and Fig. S3). Noteworthy, the in-plane lattice parameters of a V_2O_3(0001) surface and graphene commensurate very well with a ratio close to $a_{V2O3} \approx 2a_C$. According to our calculations, the only stable type of V_2O_3(0001) surface appears as stoichiometric surface with the V atoms moved inward to the surface layer. The graphene sheet can stay 3.1 Å away from this reconstructed surface.

Despite the exclusively thermodynamic characterization, the calculations are capable to explain the origin of several morphological features established in the experimentally fabricated V_2O_3/C composites. Irrespective of the mechanism for reduction of V^{5+} from metal-organic precursors, the formation of any vanadium carbides, vanadium oxycarbides or stable $(V,C)_2O_3$ solid solutions within the V_2O_3/C system should be not expected. Any possible $(V,C)_2O_3$ intermediate should decompose into a thermodynamically more stable state, namely, the nanocavernous bulk V_2O_3 with CO or C_2 species residing in the caverns. Such structural faults do not promote the mechanical stability of the lattice and can serve as the origins of cracks with degassing of fugitive components. The higher the content of the faults, the smaller domains of forming V_2O_3 should be observed. After all, the most likely forms of carbon in the V_2O_3/C
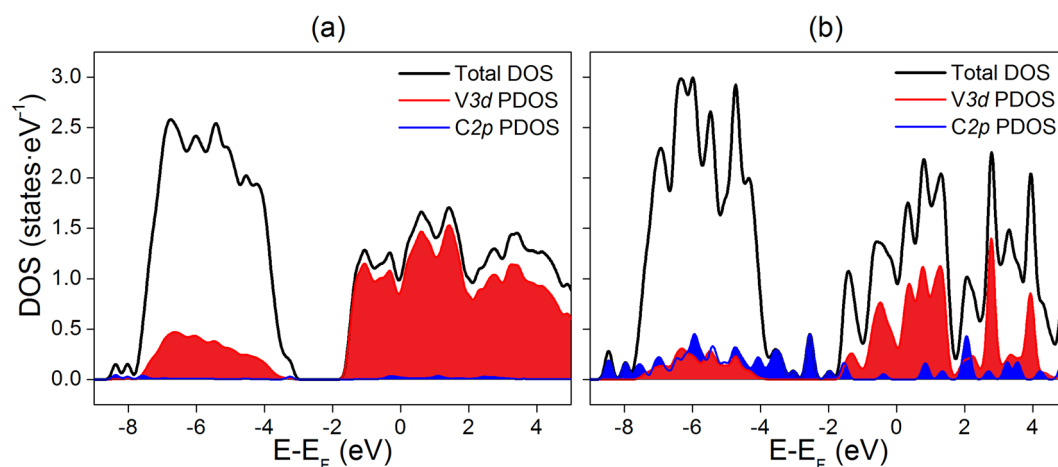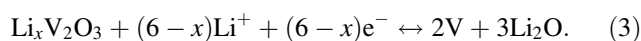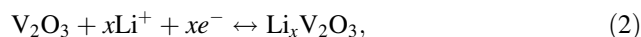
Fig. 4 Total and selected partial electronic densities-of-states (DOS) for a couple of V_2O_3/C composites: **a** the bulk V_2O_3 with a nanocavern hosting CO molecules (initially, carbon was hosted in the V sublattice); **b** model interface of stoichiometric $V_2O_3(0001)$ surface and graphene, the DOS of V3d states is depicted only for the surface atoms. DFTB calculations

composites are represented at the particles' surface either as carbonate groups or as elemental carbon like graphene or carbyne assembled from acetylide species.

In addition, the calculations give a preliminary estimate of the electronic structure of V_2O_3/C composites. The electronic densities-of-states (DOS) are typical for the metal-like compounds, and the origin of the DOS near the Fermi level remains similar irrespective of the carbon type in a composite. It is contributed mostly from the V3d-states of the V_2O_3 part. The examples for the most thermodynamically stable V_2O_3/C composites—with either chemically integrated or elemental carbon—are depicted in Fig. 4. Similarly to the pristine V_2O_3, the Fermi level is hosted in a local DOS minimum of the wide V3d-band, hence, all composites should have a metal-like conductivity. Valence O2p states form the wide band at $-8...-4$ eV below the Fermi level. Chemically integrated carbon (like molecular-like CO or C_2) donates also occupied C2p states to both the top and the bottom of the main valence band (Fig. 4a). In the case of physisorbed carbon like graphene in contact to the $V_2O_3(0001)$ surface, the valence C2p states demonstrate an essential dispersion, though, they are missing at the Fermi level (Fig. 4b). Here, V3d states near the Fermi level are presented by both the bulk and the surface V atoms. Thus, all V_2O_3/C composites should preserve a metal-like type of conductivity like parent V_2O_3.

Electrochemical properties of the V_2O_3/C composites synthesized with different carbon sources are investigated by cyclic voltammetry (CV) and galvanostatic cycling with potential limitation (GCPL) in the voltage range between 0.01 V and 3.2 V. Exemplary for all samples, Fig. 5a shows the first, second, and fifth cycle of the cyclic voltammogram of V_2O_3/C-M recorded at a scan rate of 0.05 mV s^{-1}. As shown in Fig. S4, the CV curves of the other two composites, V_2O_3/C-C and V_2O_3/C-T, exhibit the same features.

Starting with a reductive scan in the first cycle a peak R_{SEI} at around 0.75 V occurs mainly due to the irreversible formation of a solid electrolyte interface (SEI) [21]. The redox peak pair R_C/O_C around the lower limit 0.01 V corresponds to the lithiation and delithiation of the carbon [44]. All other features, the reduction peaks R_1 and R_2 as well as the oxidation peaks $O1$ and $O2$, can be assigned to the electrochemical reactions of V_2O_3. The Li$^+$ storage of V_2O_3 initially runs via intercalation (Eq. 2) and, subsequently, conversion of Li$_x$V$_2$O$_3$ to metallic V and Li$_2$O (Eq. 3) as follows [2, 45]:

$$V_2O_3 + x\text{Li}^+ + xe^- \leftrightarrow \text{Li}_x\text{V}_2\text{O}_3, \tag{2}$$

$$\text{Li}_x\text{V}_2\text{O}_3 + (6-x)\text{Li}^+ + (6-x)\text{e}^- \leftrightarrow 2\text{V} + 3\text{Li}_2\text{O}. \tag{3}$$

In the CV curve, there are two broad reduction peaks at 0.9 and 1.75 V and two oxidation peaks at 1.25 and 2.5 V. The absence of much more pronounced peaks implies that the de-/lithiation process smoothly proceeds with several transition species originating from the multivalence of vanadium [21, 46].

The cycling performances of the different samples are studied by GCPL measurements. In Fig. 5b, the dis-/charge capacities at 100 mA g^{-1} are shown. The first dis-/charge capacities of V_2O_3/C-C, V_2O_3/C-M, and V_2O_3/C-T are 769/302, 763/358, and 612/257 mAh g^{-1}, respectively. The huge discrepancy between the first discharge and charge capacity is caused by the irreversible SEI formation and structural changes during the first lithiation [2, 7, 24]. Upon further cycling, the capacity initially rises slightly, which can be attributed to an activation process as a result of electrochemical grinding. This phenomenon has been observed in literature for V_2O_3-based electrodes [7, 21] as
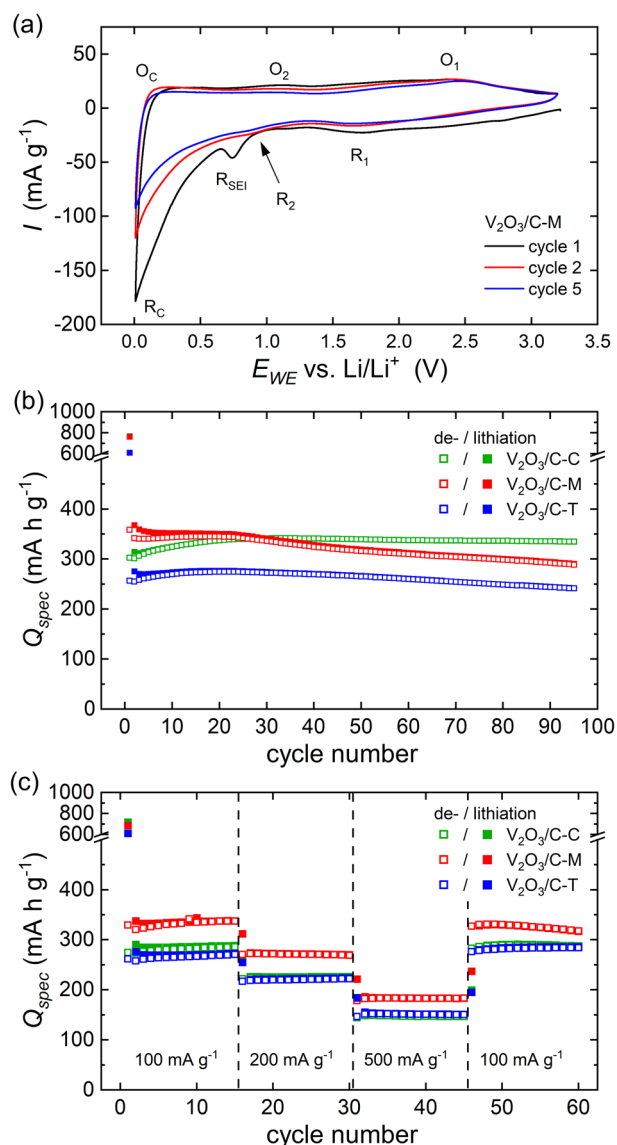
Fig. 5 **a** CV curves of V_2O_3/C-M recorded at a scan rate of 0.05 mV s^{-1}. **b** Specific dis-/charge capacities during galvanostatic cycling at 100 mA g^{-1} and **c** rate capability at various current densities of 100, 200, and 500 mA g^{-1} of the composites fabricated using citric acid (V_2O_3/C-C), malic acid (V_2O_3/C-M), and tartaric acid (V_2O_3/C-T)

well as other anode materials [47, 48]. During the whole measurement the samples exhibit a high cycle stability, whereas especially V_2O_3/C-C stands out. It convinces with a capacity retention of 98% in cycle 95 relative to cycle 33, where the maximal charge capacity of 342 mAh g^{-1} is obtained. By comparing the composites among each other no clear differences of the electrochemical performance can be observed. As expected, due to the quite similar physical properties of the different composites, the used carbon source (citric acid, malic acid or tartaric acid) does not strongly affect the electrochemical properties. In Fig. 5c, the specific dis-/charge capacities are shown at different current rates between 100 and 500 mA g^{-1}. The composite

V_2O_3/C-M is superior and exhibits specific charge capacities of 337, 269, and 183 mAh g^{-1} at current densities of 100, 200, and 500 mA g^{-1} after 15 cycles each. When the current density is returned to 100 mA g^{-1} a charge capacity of 327 mAh g^{-1} is regained, demonstrating excellent capacity retention. The other two samples also exhibit high rate performance. The dis-/charge profiles (Fig. S5b) reveal no significant differences of the overpotential due to polarization effects for the different composites. The slightly better rate capacity of V_2O_3/C-M compared to V_2O_3/C-T may be due to an improved electronic conductivity of the material. The percolation threshold for forming a conductive network in a randomly packed three-dimensional body consisting of conductive and insulating particles is exceeded by the higher carbon content, which ensures higher conductivity in the V_2O_3/C-M composite, and thus achieves superior performance [49, 50]. The fact that the composite V_2O_3/C-C with the highest carbon content shows lower rate capacity as V_2O_3/C-M might be due the less amount of the active material, V_2O_3, in the anode material that comes along with it [49].

For a comparison, the electrochemical performances of V_2O_3/C composites prepared via different synthesis methods are collected in Table 2. It can be concluded that the composites presented in this work lie in the midfield. The outstanding performance of V_2O_3/C nanocomposites prepared through the thermolysis of a polymer matrix-based metal precursor can possibly be explained by the good distribution of both components.

4 Conclusions

In summary, we demonstrate a facile, low cost, and scalable two-step route to fabricate pure vanadium-based V_2O_3/C composites of polynanocrystalline V_2O_3 microparticles encapsulated in an amorphous carbon matrix. The absence of foreign phases is confirmed by means of several physical and analytical methods, while the existence of the few-atom impurities has been criticized using quantum-chemical calculations. Based on theoretical analysis, the formation mechanism of such structured composites might include formation of molecular CO, carbonate ions and progressive growth of C–C chains all upon carbonization of precursors. Diffusion out of decomposing precursor and outgassing of these species leads to extensive fracturing of emerging V_2O_3 lattice and to the elemental carbon remained at surface of V_2O_3.

A slight regulation of the carbon content, the typical size of V_2O_3 nanocrystallites and, consequently, the accessible physical surface of the product can be attained using different precursors—vanadyl complexes with citric, tartaric, or malic acids. However, electrochemical performance of

Table 2 Comparison of the electrochemical performance of V_2O_3/C electrodes prepared via different synthesis methods as reported in the literature

Material	Method of synthesis[a]	Current density (mA g^{-1})	1st charge capacity (mAh·g^{-1})	Specific capacity (mAh g^{-1})/cycle no.	Ref.
V_2O_3/C particles	Polymer-pyrolysis	200	800	780/100	[21]
V_2O_3 nanoplatelets/C with core-shell structure	Hydrothermal	100	360[b]	260/100	[4]
Yolk-shell V_2O_3/C microspheres	Solvothermal	100	470[b]	437.5/100	[13]
3D V_2O_3/C networks	Freeze-drying	1000	450[b]	580/500	[17]
V_2O_3/C nanoparticles	Solvothermal	200	380	525/200	[7]
Dandelion-like V_2O_3/C spheres	Solvothermal	500	280[b]	474/400	[23]
Peapod-like V_2O_3/C nanowires	Hydrothermal	100	230	186/125	[11]
V_2O_3/C microparticles	Sol–gel thermolysis	100	302	335/95	This work

[a]All mentioned synthesis methods include a post heat treatment

[b]Values are estimated from the graphs

the final products as anode materials for LIBs are not strongly affected by the type of carbon source. Slight differences in the rate capacity may be due to different carbon contents. All our V_2O_3/C composites exhibit an excellent cycle stability at a medium-range reversible capacity in-line with formerly known V_2O_3/C composites.

Compliance with ethical standards

Conflict of interest The authors declare no competing interests.

References

1. Adler D, Feinleib J (1964) Semiconductor-to-metal transition in V_2O_3. Phys Rev Lett 12:700

2. Li H, Balaya P, Maier J (2004) Li-storage via heterogeneous reaction in selected binary metal fluorides and oxides. J Electrochem Soc 151:A1878–A1885

3. Sun Y, Jiang S, Bi W, Wu C, Xie Y (2011) Highly ordered lamellar V_2O_3-based hybrid nanorods towards superior aqueous lithium-ion battery performance. J Power Sources 196:8644–8650

4. Cheng W, Zeng G, Niederberger M (2015) Design of vanadium oxide core–shell nanoplatelets or lithium ion storage. J Mater Chem A 3:2861–2868

5. Leng J, Mei H, Zhan L, Wang Y, Yang S, Song Y (2017) V_2O_3 nanoparticles anchored onto the reduced graphene oxide for superior lithium storage. Electrochim Acta 231:732–738

6. Zeng L, Zheng C, Xi J, Fei H, Wei M (2013) Composites of V_2O_3–ordered mesoporous carbon as anode materials for lithium-ion batteries. Carbon 62:382–388

7. Huan C, Zhao X, Xiao X, Lu Y, Qi S, Zhan Y, Zhang L, Xu G (2019) One-step solvothermal synthesis of V_2O_3@C nanoparticles as anode materials for lithium-ion battery. J Alloys Compd 776:568–574

8. Gou W, Kong X, Wang Y, Ai Y, Liang S, Pan A, Cao G (2019) Yolk-shell structured V_2O_3 microspheres wrapped in N, S co-doped carbon as pea-pod nanofibers for high-capacity lithium ion batteries. Chem Eng J 374:545–553

9. Zhang D, Li G, Li B, Fan J, Liu X, Chen D, Li L (2019) A facile strategy to fabricate V_2O_3/porous N-doped carbon nanosheet framework as high-performance anode for lithium-ion batteries. J Alloy Compd 789:288–294

10. Han C, Liu F, Liu J, Li Q, Meng J, Shao B, He Q, Wang X, Liu Z, Mai L (2018) Facile template-free synthesis of uniform carbon-confined V_2O_3 hollow spheres for stable and fast lithium storage. J Mater Chem A 6:6220–6224

11. Li X, Fu J, Pan Z, Su J, Xu J, Gao B, Peng X, Wang L, Zhang X, Chu PK (2016) Peapod-like V_2O_3 nanorods encapsulated into carbon as binder-free and flexible electrodes in lithium-ion batteries. J. Power Sources 331:58–66

12. Liu H, Wang Y, Li H, Yang W, Zhou H (2010) Flowerlike vanadium sesquioxide: solvothermal preparation and electrochemical properties. ChemPhysChem 11:3273–3280

13. Jiang L, Qu Y, Ren Z, Yu P, Zhao D, Zhou W, Wang L, Fu H (2015) In situ carbon-coated yolk-shell V_2O_3 microspheres for lithium-ion batteries. ACS Appl Mater Interfaces 7:1595–1601

14. Wang J, Liu Z, Yang W, Han L, Wei M (2018) A one-step synthesis of porous V_2O_3@C hollow spheres as a high-performance anode for lithium-ion batteries. Chem Commun 54:7346–7349

15. Bai Y, Tang Y, Liu L, Li X, Gao Y (2018) Peapod-like CNT@V_2O_3 with superior electrochemical performance as an

anode for Li-ion batteries. ACS Sustain Chem Eng 6:14614–14620

16. Yu P, Liu X, Wang L, Tian C, Yu H, Fu H (2017) Urchin-like V_2O_3/C hollow nanosphere hybrid for high-capacity and long-cycle-life lithium storage. ACS Sustain Chem. Eng 5:11238–11245

17. Ren X, Ai D, Zhan C, Lv R, Kang F, Huang Z-H (2019) NaCl-template-assisted freeze-drying synthesis of 3D porous carbon encapsulated V_2O_3 for lithium-ion battery anode. Electrochim Acta 318:730–736

18. Gao S, Zhang D, Zhu K, Tang JA, Gao Z, Wei Y, Chen G, Gao Y (2017) Flexible V_2O_3/carbon nano-felts as free-standing electrode for high performance lithium ion batteries. J Alloy Compd 702:13–19

19. Zhang Y, Pan A, Liang S, Chen T, Tang Y, Tan X (2014) Reduced graphene oxide modified V_2O_3 with enhanced performance for lithium-ion battery. Mater Lett 137:174–177

20. Liu X, Zhang D, Li G, Xue C, Ding J, Li B, Chen D, Li L (2018) In situ synthesis of V_2O_3 nanorods anchored on reduced graphene oxide as high-performance lithium ion battery anode. Chem Select 3:12108–12112

21. Dong Y, Ma R, Hu M, Cheng H, Lee J-M, Yang Li Y, Zapien JA (2014) Polymer-pyrolysis assisted synthesis of vanadium trioxide and carbon nanocomposites as high performance anode materials for lithium-ion batteries. J Power Sources 261:184–187

22. Xiao B, Zhang B, Tang L, An C, He Z, Tong H, Yu W, Zheng J (2018) V_2O_3/rGO composite as a potential anode material for lithium ion batteries. Ceram Int 44:15044–15049

23. Xun L, Gao S, Xu Y, Cheng X, Zhang X, Zhao H, Huo L (2018) Synthesis of dandelion-like V_2O_3/C composite with bicontinuous 3D hierarchical structures as an anode for high performance lithium ion batteries. Ceram Int 44:14128–14135

24. Shi Y, Zhang Z, Wexler D, Chou S, Gao J, Abruňa HD, Li H, Liu H, Wu Y, Wang J (2015) Facile synthesis of porous V_2O_3/C composites as lithium storage material with enhanced capacity and good rate capability. J Power Sources 275:392–398

25. Priyadharsini N, Kasturi PR, Shanmugavani A, Surendran S, Shanmugapriya S, Selvan RK (2018) Effect of chelating agent on the sol–gel thermolysis synthesis of $LiNiPO_4$ and its electrochemical properties for hybrid capacitors. J Phys Chem Solids 119:183–192

26. Yin Y, Zhang B, Zhang X, Xu J, Yang S (2013) Nano $MgFe_2O_4$ synthesized by sol–gel auto-combustion method as anode materials for lithium ion batteries. J Sol–Gel Sci Technol 66:540–543

27. Mączk M, Pasier P (2019) Sol–gel synthesis of metal (V, W, Zn) oxide - Carbon nanocomposites as cathode materials for Al-ion batteries. Ceram Int 45:11041–11049

28. Gangulibabu, Bhuvaneswari D, Kalaiselvi N, Jayaprakash N, Periasamy P (2009) CAM sol–gel synthesized $LiMPO_4$ (M=Co, Ni) cathodes for rechargeable lithium batteries. J Sol–Gel Sci Technol 49:137–144

29. Porezag D, Frauenheim TH, Köhler TH, Seifert G, Kaschner R (1995) Construction of tight-binding-like potentials on the basis of density-functional theory: application to carbon. Phys Rev B 51:12947

30. Elstner M, Porezag D, Jungnickel G, Elsner J, Haugk M, Frauenheim TH, Suhai S, Seifert G (1998) Self-consistent-charge density-functional tight-binding method for simulations of complex materials properties. Phys Rev B 58:7260

31. Jähne C, Neef C, Koo C, Meyer H-P, Klingeler R (2013) A new $LiCoPO_4$ polymorph via low temperature synthesis. J Mater Chem A 1:2856–2862

32. Vaqueiro P, López MA (1997) Quintela, Influence of complexing agents and pH on yttrium-iron garnet synthesized by the sol–gel method. Chem Mater 9:2836–2841

33. Dupont A, Parent C, Le Garrec B, Heintz JM (2003) Size and morphology control of Y_2O_3 nanopowders via a sol–gel route. J Solid State Chem 171:152–160

34. Zheng F, Ou X, Pan Q, Xiong X, Yang C, Liu M (2017) The effect of composite organic acid (citric acid & tartaric acid) on microstructure and electrochemical properties of $Li_{1.2}Mn_{0.54}Ni_{0.13}Co_{0.13}O_2$ Li-rich layered oxides. J Power Sources 346:31–39

35. Wang D, Cao L, Huang J, Wu J (2013) Effects of different chelating agents on the composition, morphology and electrochemical properties of LiV_3O_8 crystallites synthesized via sol–gel method. Ceram Int 39:3759–3764

36. Ramana CV, Smith RJ, Hussain OM, Julien CM (2004) Growth and surface characterization of V_2O_5 thin films made by pulsed-laser deposition. J Vac Sci Technol A 22:2453–2458

37. Xu G, Wang X, Chen X, Jiao L (2015) Facile synthesis and phase transition of V_2O_3 nanobelts. RSC Adv 5:17782–17785

38. Ferrari AC, Robertson J (2000) Interpretation of Raman spectra of disordered and amorphous carbon. Phys. Rev. B 61:14095–14107

39. Ferrari AC, Basko DM (2013) Raman spectroscopy as a versatile tool for studying the properties of graphene. Nature nanotechnology 8:235–246

40. Merlen A, Buijnsters J, Pardanaud C (2017) A guide to and review of the use of multiwavelength Raman spectroscopy for characterizing defective aromatic carbon solids: from graphene to amorphous carbons. Coatings 7:153

41. Ferreira EHM, Moutinho MVO, Stavale F, Lucchese MM, Capaz RB, Achete CA, Jorio A (2010) Evolution of the Raman spectra from single-, few-, and many-layer graphene with increasing disorder. Phys Rev B 82:125429

42. Cancado LG, Jorio A, Ferreira EHM, Stavale F, Achete CA, Capaz RB, Moutinho MVO, Lombardo A, Kulmala TS, Ferrari AC (2011) Quantifying defects in graphene via Raman spectroscopy at different excitation energies. Nano Lett 11:3190–3196

43. Sing KSW, Everett DH, Haul RAW, Moscou L, Pierotti RA, Rouquerol J, Siemieniewska T (1985) Pure Appl Chem 57:603–619

44. Ottmann A, Scholz M, Haft M, Thauer E, Schneider P, Gellesch M, Nowka C, Wurmehl S, Hampel S, Klingeler R (2017) Electrochemical magnetization switching and energy storage in manganese oxide filled carbon nanotubes. Sci Rep 7:13625

45. Tranchant A, Messina R, Perichon J (1980) Mechanism of electrochemical reduction of vanadium oxides. J Electroanalyt Chem Interfacial Electrochem 113:225–232

46. Wang Y, Zhang HJ, Admar AS, Luo J, Wong CC, Borgna A, Lin J (2012) Improved cyclability of lithium-ion battery anode using encapsulated V_2O_3 nanostructures in well-graphitized carbon fiber. RSC Adv 2:5748–5753

47. Dong Y, Ma R, Hu M, Cheng H, Yang Q, Li YY, Zapien JA (2013) Thermal evaporation-induced anhydrous synthesis of Fe_3O_4-graphene composite with enhanced rate performance and cyclic stability for lithium ion batteries. Phys Chem Chem Phys 15:7174–7181

48. Zhu T, Chen JS, Lou XW(D) (2011) Glucose-assisted one-pot synthesis of FeOOH nanorods and their transformation to Fe_3O_4@carbon nanorods for application in lithium ion batteries. J Phys Chem C 115:9814–9820

49. Wang C, Sawicki M, Emani S, Liu C, Shaw LL (2015) Na3MnCO3PO4—a high capacity, multi-electron transfer redox cathode material for sodium ion batteries. Electrochim Acta 161:322–328

50. Rajkumar P, Diwakar K, Subadevi R, Gnanamuthu RM, Wang F-M, Liu W-R, Sivakumar M (2021) Graphene sheet-encased silica/sulfur composite cathode for improved cyclability of lithium-sulfur batteries. J. Solid State Electrochem 25:939–948